

Emulation-Based Calibration for Parameters in Parameterized Phonon Spectrum of ZrH_x in TRIGA Reactor Simulations

Weixiong Zheng^a, Ryan G. McClarren^{a,*}

^a*Department of Nuclear Engineering, Dwight Look College of Engineering, Texas A&M
University, College Station, TX 77843-3133*

Abstract

We investigate the calibration of the uncertainties of thermal scattering of ZrH_x in the fuel material in TRIGA reactor simulations. Thermal scattering cross sections of ZrH_x are heavily affected by the solid-state frequency distributions, also called “phonon spectra”. In previous work, we have proposed parameterized phonon spectrum models and explored the effects on quantities of interest (QoIs) of changing spectra with such models by varying the parameters. In this work we establish a more general calibration framework for the phonon spectrum of ZrH_x . To accomplish this calibration we introduce two emulators: Gaussian process regression and Bayesian multivariate adaptive regression splines, to create a map from the input parameters to the QoIs into the calibration framework. Using these emulators we perform calibrations using the emulation results with the same QoIs at 600 K. Test simulations using data generated with calibrated parameters show that uncertainties of the QoIs shrink over 50%. Moreover, we extend the test to the reactivity at a different temperature, 293.6 K, as an extrapolated test of the calibration, and obtained close results to the surrogate experiment. The efficacy and efficiency of implementing emulators in the calibration framework are demonstrated.

Keywords: Phonon spectrum, Thermal neutron scattering, Uncertainty

*Corresponding author

Email addresses: zwxne2010@tamu.edu (Weixiong Zheng), rgm@tamu.edu (Ryan G. McClarren)

1. Introduction

1.1. Background and Motivation

TRIGA reactors, such as the one located at Texas A&M Nuclear Science Center, use U-ZrH_x as fuel and make use of its moderation and thermal properties[1].

5 At thermal energies, the neutron scattering from ZrH_x is heavily affected by the phonon spectra of H and Zr in ZrH_x. These phonon spectra are determined by the solid structures of ZrH_x. Different solid structures in a bound system, like ZrH_x, leads to a different chemical binding of atoms in the scatterer molecules; this in turn affects the scattering of a thermal neutron through changes to the
10 phonon spectra.

Current data libraries, e.g. ENDF-VII, are based on the structure of ZrH₂ [2, 3, 4]. It has been shown experimentally that changes in H concentration, x in ZrH_x, cause changes in the solid structure of ZrH_x [5, 6]. These different solid structures of ZrH_x result in different phonon spectra, and, as a result,
15 could cause the data in existing libraries to be insufficient for simulation of some reactor systems.

Previous research has investigated the effects on phonon spectra brought by ZrH_x compositions and found or established proper phonon spectra for some specific type of ZrH_x. For instance, Malik et al. derived a three-Gaussian model
20 for the optical mode of H spectrum and found optimal sets of parameters constructing the optical mode leading to good agreement with experimental measurements[5]. Later, Badea et al. performed simulations on a TRIGA reactor with shifting peak positions of the H spectrum of ZrH_x and observed effects on criticality calculations, a result of which is one of the foundations of
25 methodology and model construction in this work [7].

The H concentration of ZrH_x at Texas A&M Nuclear Science Center is 1.523 [1], which would result in different phonon spectra from existing spectra. We therefore derived parameterized phonon spectrum (PPS) models for phonon

spectra of H and Zr in ZrH_x based on Mattes's Debye-plus-Gaussian (DG)
 30 model[8] for H in ZrH_x , inspired by its good agreement with experimental re-
 sults and simple mathematical formula such that we could explore the effects
 introduced by varying parameters[9, 10, 11]. We desire to develop a general
 framework for calibrating phonon spectrum models for ZrH_x . We then can use
 experimental data to construct a response surface, or emulator, that can be used
 35 to tune the model to match one or several measured, experimental results.

The goal of this paper, and the goal of calibration in general, can be de-
 scribed as: given experimental results on a specific TRIGA reactor, surrogate
 or realistic, we seek an optimal set(s) of parameters constructing PPS model(s)
 such that the data generated with such model(s) would result in comparably
 40 accurate simulation results to the experiments. To this end, in the remainder
 of this section we discuss the theory and previous work in developing phonon
 spectra models for ZrH_x . In Section 2 we then describe the procedure of cal-
 ibration to experiments, and then differentiate this into the process of direct
 calibration (Section 3) and emulation-based calibration (Section 4). We then
 45 test our emulation-based calibration framework in Section 5 before concluding
 our analysis.

1.2. Theory and previous work

Theory

In the ZrH_x bound system, the double differential scattering cross section at
 thermal energies can be given (as in, for example, Chapter 7 in[12]):

$$\sigma(E' \rightarrow E, \mu) = \frac{\hat{\sigma}_b}{2kT} \sqrt{\frac{E}{E'}} S(\alpha, \beta), \quad (1)$$

where E' and E are the incident and secondary neutron energies and $\hat{\sigma}_b$ is
 the characteristic scattering cross section of the bound system. The function
 $S(\alpha, \beta)$ is named thermal scattering law, where α and β are defined by:

$$\alpha \equiv \frac{E + E' - 2\mu\sqrt{EE'}}{AkT} \quad \text{and} \quad \beta \equiv \frac{E - E'}{kT}. \quad (2)$$

α and β are the momentum and energy transfer, respectively. A represents the ratio of the scatterer (such as H in ZrH_x) mass to neutron mass. The scattering law can be expressed as:

$$S(\alpha, \beta) = \int_{-\infty}^{\infty} e^{i\beta\hat{t}} e^{-\gamma(\hat{t})} d\hat{t}, \quad (3)$$

where \hat{t} is a non-dimensional time which is measured in units of \hbar/kT . $\gamma(\hat{t})$ is given by:

$$\gamma(\hat{t}) = \alpha \int_{-\infty}^{\infty} \frac{f(\beta)}{2\beta \sinh(\beta/2)} \left[1 - e^{-i\beta\hat{t}} \right] e^{-\beta/2} d\beta, \quad (4)$$

where $f(\beta)$ is the non-dimensional phonon spectrum of the bound system. The
50 phonon spectrum then connects with the scattering law and scattering cross sections via Eqs. (1), (3) and (4). It contains all the information one needs to compute the scattering data. Physically, specifying a phonon spectrum is equivalent to indicating a specific type of solid structure and the corresponding chemical bindings, and therefore the phonon spectrum specifies the scattering
55 law which determines a specific set of scattering cross sections.

Historically, some models were proposed for spectra of ZrH_x , especially the optical mode of H spectrum. Here we briefly summarize these works. Slaggie et al. developed the “centered force” model (CF) with the solid physics code GASKET for ZrH_2 [2]. This model is applied in the ENDF library. Also, Slaggie
60 suggested a simple Debye distribution¹ peaking at 20 meV plus a Gaussian distribution with a full-width at half maximum (FWHM) of 20 meV and a mean of 137 meV for the ZrH_2 molecule. Later, Malik et al. developed a three-Gaussian model for the optical mode of the H spectrum specifically for $\text{ZrH}_{1.58}$. Additionally, Evans et al. derived the optical model H spectrum by inferring
65 it from measured $S(\alpha, \beta)$ values[6]. Mattes et al. developed a new simplified model in which Zr is treated as free gas while H spectrum is composed of a Debye distribution peaking at 20 meV and a Gaussian distribution with the

¹A Debye distribution takes the form of $f(\omega) = C\omega^2$, $\omega < T_{\text{Debye}}$; $f(\omega) = 0$, $\omega \geq T_{\text{Debye}}$, where T_{Debye} is the Debye temperature and C is the normalization constant.

mean of 137 meV and a FWHM of 28 meV[8]. This model is known as the Debye-plus-Gaussian (DG) model.

70 *Parameterized phonon spectra*

Specifically, the H spectrum in the DG model is given by:

$$f(\omega)_H = \begin{cases} \frac{3}{241T_{\text{Debye}}^3}\omega^2 & \omega < T_{\text{Debye}} \\ \frac{240}{241\sqrt{2\pi}\sigma} \exp\left[-\frac{(\omega-137)^2}{2\sigma^2}\right] & T_{\text{Debye}} \leq \omega \leq \omega_{\text{max,H}}. \end{cases} \quad (5)$$

where $T_{\text{Debye}} = 20$ meV is the Debye temperature and σ is the standard deviation of the Gaussian distribution and $\sigma = \text{FWHM}/(2\sqrt{2\ln 2}) \approx 11.89$ meV. It is a combination of Debye distribution ($\omega < 20$ meV) and a Gaussian distribution ($\omega \geq 20$ meV). Since Zr is treated as a free gas molecule, the corresponding
75 spectrum is a Dirac delta function at $\omega = 0$ [4].

Though the DG phonon spectrum with such a simple mathematical form lacks the details of the CF model from solid dynamics computations, multiple experimental results demonstrate the efficacy of the model[8]. It is even said the DG model would work better than ENDF's model[8]. Inspired by these results
80 we, in recent work, developed PPS models for both H and Zr in ZrH_x based upon DG model[9, 10, 11], such that the phonon spectra can be flexibly varied by tuning parameters.

Correspondingly, the H spectrum is given by

$$f(\omega)_H = \begin{cases} \frac{3b}{2T_H^3}\omega^2 & \omega < T_H \\ \frac{3b}{2T_H^3}(\omega - 2T_H)^2 & T_H \leq \omega \leq 2T_H \\ \frac{g(b)}{\sqrt{2\pi}\sigma} \exp\left[-\frac{(\omega-p)^2}{2\sigma^2}\right] & 2T_H \leq \omega \leq \omega_{\text{max,H}}. \end{cases} \quad (6)$$

And the Zr spectrum is give by:

$$f(\omega)_{\text{Zr}} = \begin{cases} \frac{r(1+c)}{T_{\text{Zr}}^{1+c}}\omega^c & \omega < T_{\text{Zr}} \\ \frac{(1+c)r}{T_{\text{Zr}}} \exp\left[\frac{(1+c)^r}{1-r}\left(1 - \frac{\omega}{T_{\text{Zr}}}\right)\right] & T_{\text{Zr}} \leq \omega \leq \omega_{\text{max,Zr}}. \end{cases} \quad (7)$$

Note that

$$\int_0^\infty f(\omega)d\omega = \int_0^\infty f(\beta)d\beta \quad \text{and} \quad \beta = \frac{E - E'}{kT} = \frac{\omega}{kT}, \quad (8)$$

where ω is energy transfer in units of eV.

In Eq. (6), b is the branching ratio of the acoustic part with a range of
85 $[1/361, 1/91]$; T_H is the acoustic peak of H in ZrH_x ; p is the peak position of
optical peak; σ , calculated from the FWHM of the optical part, is the standard
deviation of the Gaussian distribution; the $g(b)$ is a function of b and the nor-
malization coefficient and $g(b) \approx 1 - b$. In Eq. (7), T_{Zr} is the peak position of
the spectrum; c is the power of ω for the left side of peak; r is the ratio of the
90 left part of the peak to the whole spectrum. In total, our parameterized spectra
has seven parameters: b , T_H , p , FWHM, T_{Zr} , c and r . The sampling ranges of
each parameter are listed in Table I.

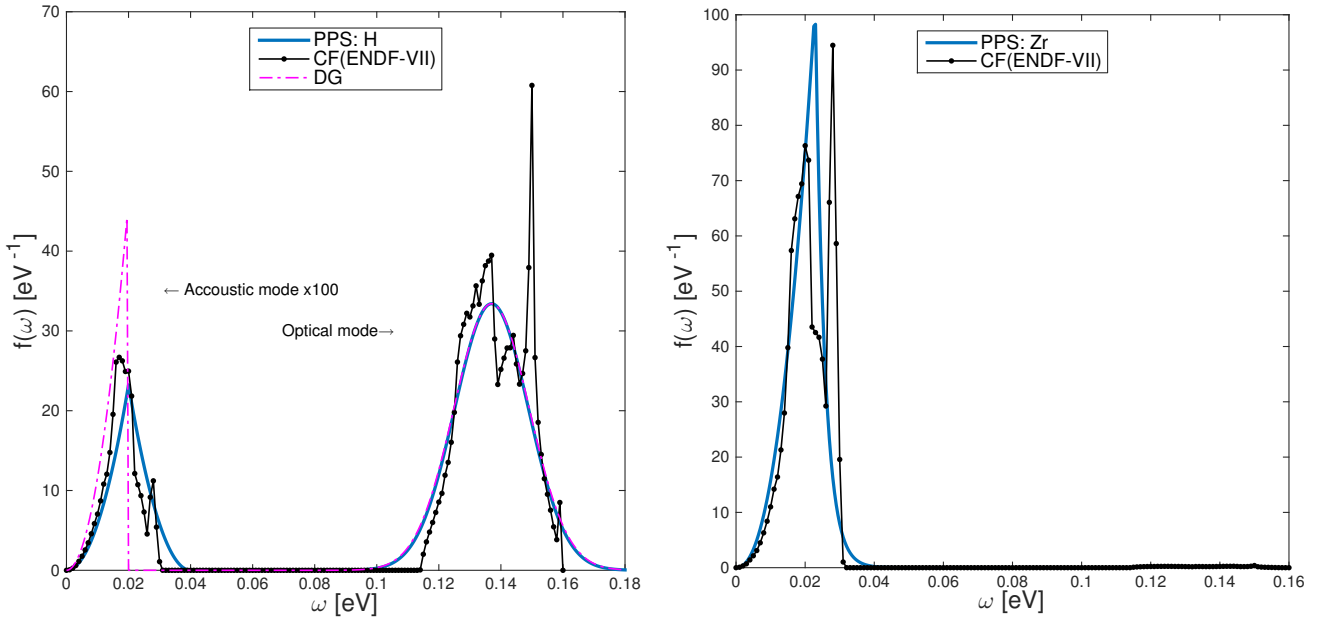
We assume a uniform distribution for each parameter in the corresponding
range. The range of b is directly taken from Slaggie's suggestion based the
95 GASKET calculation for ZrH_2 [2]. The range of T_H is set as $\pm 20\%$ of the Debye
temperature used in DG model. Setting about $\pm 10\%$ variation in FWHM leads
to the corresponding range for this parameter. The range set for p is chosen to
observe the effect from shifting the optical peak with ± 10 meV around the value
give by DG similar to Badea's numerical experiment on shifting the optical mode
100 of H in CF (ENDF-VII)[7]. Slaggie also suggested simplifying the Zr spectrum
as a Debye distribution with $T_{Debye} = 20$ meV. We simply take the Debye
temperature as a basis for the peak position of Zr PPS model and vary it by a
factor of $\pm 20\%$. c and r are shape-adjusting factors. The lower bound of c is
set to be 2 such that the integrand in Eq. (4) must have a limit when $\beta \rightarrow 0$ [4].
105 We use 3 as an upper bound of c such that the maximum magnitude of the
spectrum is reasonably bounded. r determines the attenuation of the spectrum
on the right side of the peak at T_{Zr} . There is no physical basis for the range of
 r : we set it such that the Zr PPS spectrum can present different decay speeds
when increasing ω on the right side of the peak.

110 Figure 1 shows the comparisons among DG, CF and PPS with a specific
combination of parameters. We use the same parameters as the DG model for
the H spectrum, i.e., $T_H = 20$ meV, $b = 1/241$, $p = 137$ meV and $FWHM = 28$
meV. We also set $T_{Zr} = 22.9$ meV, $c = 2.255$ and $r = 0.7168$. For the H

Table I: Ranges of the parameters

T_H [meV]	b	p [meV]	FWHM [meV]	T_{Zr} [meV]	c	r
[16, 24]	[1/361, 1/91]	[127, 147]	[25, 31]	[16, 24]	[2, 2.8]	[0.4, 0.8]

spectrum, we observe in Figure 1a that though PPS is identical to DG for the
115 optical mode, it also has the flexibility of capturing some of the features of the
CF acoustic mode. Also, with this specific combination of parameters, the Zr
PPS model can roughly match the CF model in shape and magnitude.



(a) Phonon spectra of H in ZrH_x from (b) Phonon spectra of H in ZrH_x from
CF(ENDF-VII), DG and PPS CF(ENDF-VII), and PPS

Figure 1: Phonon spectrum examples. Note that Zr spectrum in DG is not plotted. It is treated as free gas, which has a spectrum of Dirac function at $\omega = 0$ eV[3, 4].

Nevertheless, the PPS model is not limited to fitting existing phonon spec-
tra. In fact, it enables one to vary the phonon spectra in a controlled way.
120 Figure 2 shows some examples of phonon spectra of ZrH_x with parameters sam-
pled via Latin Hypercube sampling (LHS) designs in previous work[9, 10, 11].

LHS is a type of space-filling, stratified-sampling strategy[13]. For a total sample size of N with M variables, every dimension is divided into N/M strata. Samples are then generated from randomly selecting a stratum in each dimension and assuring that each stratum is only sampled once. Upon selecting a stratum, the variable is randomly sampled within that stratum. The numbers in the legends are the sequence number randomly selected in a 256 LHS design sampling. With different sets of parameters, PPS spectra are different, e.g., in peak positions and magnitudes.

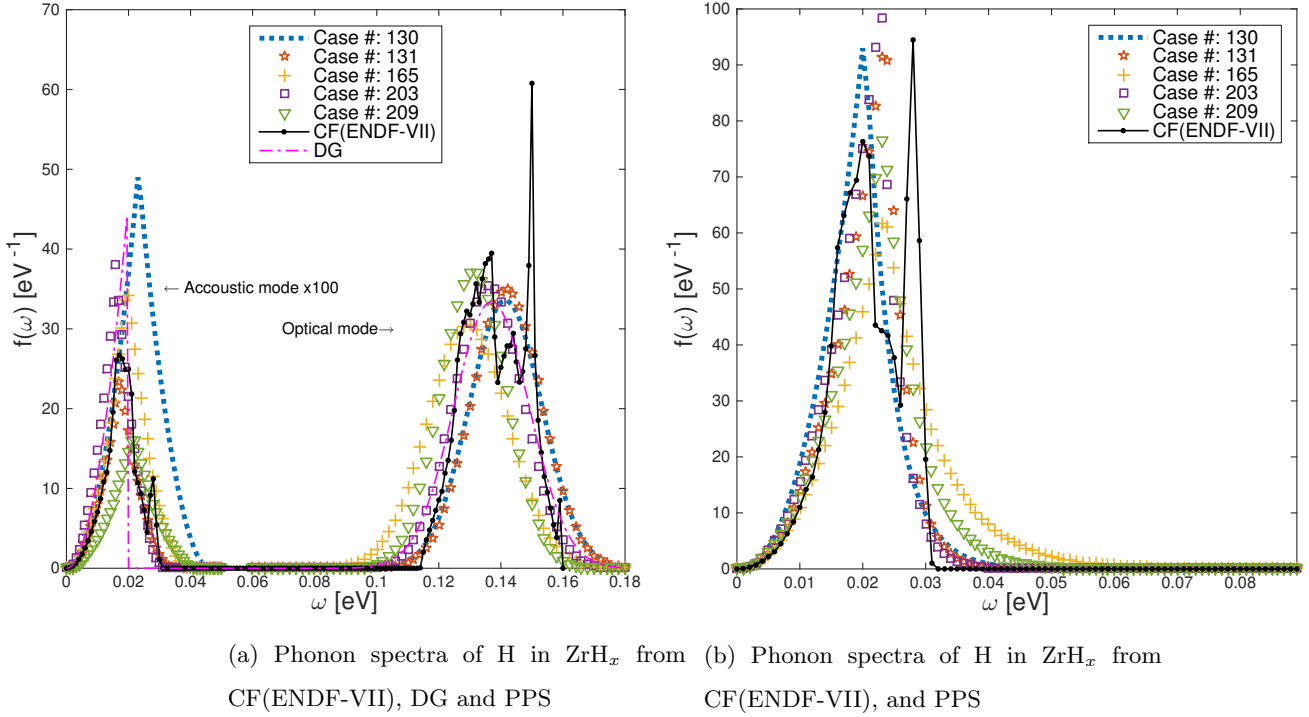


Figure 2: Comparisons among DG (H only), CF and PPS spectra.

130 Overview of our previous work

We uniformly sample parameters over the seven dimensional input space by using LHS designs. Picking a sample combination will produce a unique PPS defined by Eqs. (6) and (7), and finally, a unique set of scattering data.

Initially, we employed LHS to produce 3000 samples of parameter combinations, used NJOY[3] to generate MCNP-compatible thermal data and invoked MCNP[14] to do the criticality calculations on a TRIGA lattice geometry[9, 10]. A method combining analysis of variance (ANOVA) , with regression based cross-validation was developed to investigate the sensitivity of QoIs to parameters and the interactions between the parameters. ANOVA is a collection of statistical tests for heterogeneity of the means of outcomes by analyzing the variations of the response to each variable in a set of independent variables[15, 16, 17]. A polynomial regression with the significant parameters selected in ANOVA analysis was performed to demonstrate the efficacy of the selection[17]. The reactivity ρ was found to be sensitive to the b and p parameters and relatively insensitive to the others mentioned in Eq. (6). We refer to b and p as the two “main parameters”.

We extended the analysis to full-core TRIGA geometry with a new and effective sampling strategy using 256 samples which separately sampled the two parameters independently of the other five parameters[11]. In detail, we build one sampling design on the 2-dimensional $b - p$ space and the other design on the 5-dimensional space of the remaining parameters. The idea of this type of split-sampling is simple: we densely sample the sensitive parameters and sample the insensitive parameters in a sparse manner.

From the full core model we found the mean neutron generation time Λ and fuel temperature coefficient α , in addition to the reactivity, to be sensitive to the main parameters. Furthermore, we ran simulations with ENDF-VII thermal scattering data of ZrH_x as a surrogate of experiment and we developed a method to directly calibrate proper parameter sets to match experimental results, which will be discussed in following sections. Though ENDF-VII only has the data for ZrH_2 [3, 4], the framework is not limited to ZrH_2 : it is applicable to calibration of any type of ZrH_x or thermal scattering laws for other materials.

In this paper, we develop the calibration framework with emulators. The need for a new calibration framework is demonstrated by the fact, shown below, that to do a thorough calibration one either needs a large number of simulation

165 resultsto avoid gaps in the possible calibration result caused by lack of sample
realizations in some regions of input space. To accomplish emulator-based cali-
bration, Bayesian multivariate adaptive regression splines (BMARS) and Gaus-
sian process regression (GPR) are introduced to use inputs and corresponding
simulation outputs to produce regression models and predict on modeler-defined
170 parameter mesh points. Then we calibrate the parameters with both the direct
calibration method and emulation based methods, predictions of which are in-
formed by probability distributions and calibrate the parameters. We then test
the calibrated parameters.

2. Description of the “experiment”, the simulations and the frame- 175 work

2.1. Surrogate experiment

We run simulations with ENDF-VII thermal data for ZrH_x as a surrogate
of a real experiment. The QoIs generated from the “experimental” simulations
could be treated as experimental results.

180 The simulations for the surrogate experiments are with the full core config-
uration of the TRIGA reactor at Texas A&M University. The geometry, specifi-
cally the shim safety rod positions, is set to make the reactor to be near critical
for a 600 K fuel temperature.

2.2. Calibration framework

185 Under the same condition as the surrogate experiment, we ran 256 MCNP
simulations. In addition, another 256 runs were taken with the same geomet-
rical configuration but a different fuel temperature at 293.6 K to explore the
temperature effects. In each criticality calculation 7.5×10^7 particles were used
in total with which the standard deviation of the k_{eff} was about 10 pcm for all
190 simulations.

The basic framework of this type of UQ work is shown in Figure 3. From
Step 1 through 4, the PPS parameters are sampled via an LHS design and

propagated through phonon spectra synthesis and data generation to simulation results. In Step 5, the modeler needs to calibrate plausible PPS parameter values (or value sets) using PPS-calculated QoIs generated in Step 4 with surrogate QoIs based on ENDF data. For this work, we also have one more step for testing the calibrated PPS parameters. The expectation is that with the calibrated parameters, we should replicate experimental results.

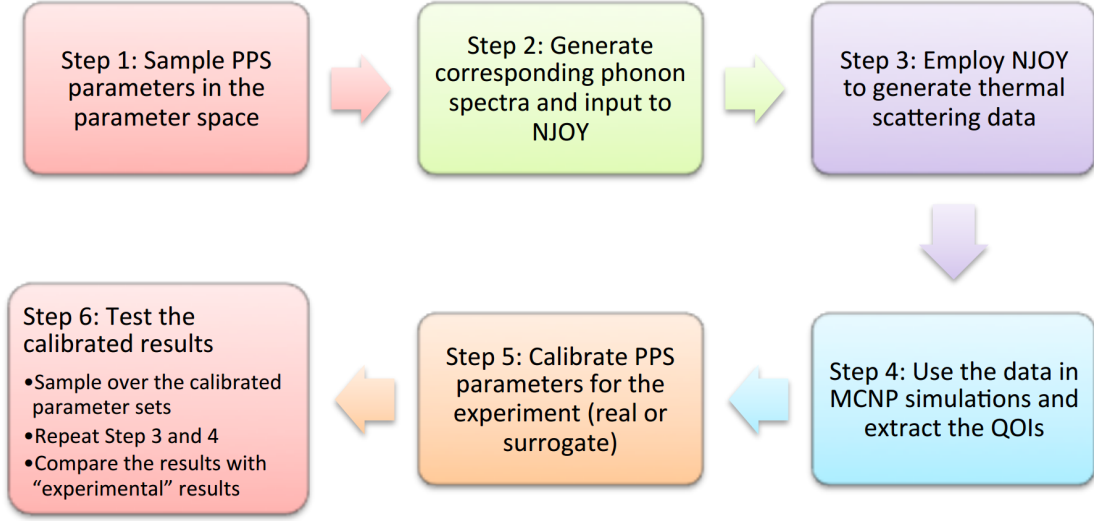


Figure 3: The flow chart of calibration framework.

In this article, we introduce several calibration techniques applied in Step 5. The performances of the techniques will be compared and shown in the following sections.

2.3. Sampling of parameters

Sampling of parameters, including uncalibrated and calibrated, are sampled via LHS design. However, in our case, sampling over seven parameters with one single equal weight would not be economical since each parameter has a distinct significance. An improved sampling strategy is to base the sampling strategy on the significances of the parameters. Fortunately, in previous work, it has been revealed that only two parameters significantly affect the QoIs.

Therefore we sample the significant two parameters separated from the other
 210 five through two LHS designs. One example of a design matrix of sampling
 50 realizations using two LHS designs are shown in Figure 4. In this figure
 below the diagonal we show a 2-D projection of the samples of each pair of
 parameters. Despite the fact that we sample the important parameters (b and
 p) more densely, the sample distributions for the other five are still appear
 215 uniform. The diagonal shows the histogram of each parameter. The magnitude
 of all bins in each histogram are almost equal, indicating the 1D projection of
 the sampling of each parameters is almost uniform on its own axis despite the
 samples are generated in multi-dimensional spaces. Above the diagonal we print
 the pair-wise correlation coefficients for each pair of parameters. Since all the
 220 absolute values of correlation coefficients are smaller than 0.3, the correlations
 can be considered small such that each parameter is sampled independently[18].

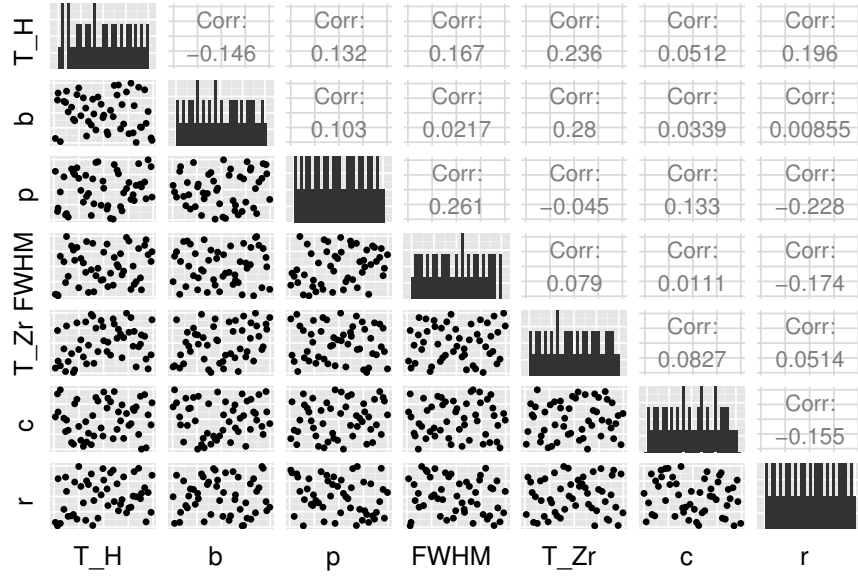


Figure 4: LHS design matrix with 50 samples.

3. Direct calibration

One could accomplish the goal of calibration via measuring how close the simulation results (outputs) are to the target or experimental results and collecting parameter sets with which one could construct phonon spectra and generate scattering data to make the simulation results close to the experiment. We name the measure process “scoring”. The scoring process requires a quantitative measure of agreement between simulation and experiment. MCNP generates QoIs as normal distributions with an estimated mean and standard deviation. Assuming the experimental results are also given in this form², then the score could be defined as the overlap between realization and measured normal distributions, as the example illustrated in Figure 5. In the example, two Gaussian distributions intersect with each other and the shadow is the overlap. We, thereafter, analytically compute the overlap for all realization of simulations to archive the scores and project the scores into the PPS parameter space. The “spatial” distribution of the scores in the parameter space indicates parameters that give good agreement with the target output. The simulation results are made with scattering data based on the phonon spectra constructed with the PPS parameters. The expectation is that the collection from all high-score realizations could form a subset of parameters in the parameter space such that simulation with ZrH_x thermal scattering data generated with those parameter subsets would be accurate compared with the measured or experimental results.

For each type of QoI, we can estimate the distribution of the scores once. Figure 6a is the example of scoring with the reactivity ρ . Since previous studies [9, 11] showed only b , the branching ratio of acoustic mode of H in ZrH_x, and p , the peak position of optical mode of H, to be the sensitive parameters, in this study all calibrations focus on these two parameters and the scores are only projected into the b - p 2D parameter space³

²Surrogate experiments performed in MCNP naturally suit this assumption.

³Interested readers may refer to Ref. [17] for a more detailed explanation of this process. The physical significance of these two parameters can be explained as follows. Slaggie’s solid

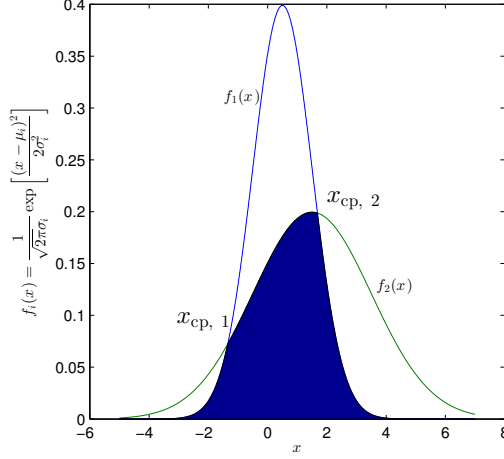


Figure 5: Example of the score estimation.

Moreover, when scoring with multiple types of QoIs simultaneously, the mul-
 250 tiplication of the score distributions narrows the size of the parameter subset.
 Figure 6b is made with scoring with ρ , Λ and α , which shows the most likely
 values of b and p reproducing the surrogate experiment plausibly. In theses
 results most likely appropriate b is about 0.01 and p is about 137 meV.

4. Emulation-based calibration

255 The direct calibration succeeds in finding preferred parameter subsets as il-
 lustrated in Figure 6. However, due to the sparseness of the calibrated results
 caused by the relatively small size of samples (256), it has the drawback that

mechanics model is based on four constants describing four types of inter-atomic interactions
 in ZrH_x molecules[2]. It indicates that changing the constant that describes the Zr-Zr interac-
 tions would cause the change in the acoustic mode magnitude, or equivalently, the branching
 ratio b . Conversely, changing b can have the same effect as changing the impact from Zr-Zr
 interactions in the solid. The p parameter represents the excitation state of the optical mode.
 It can be realized that, varying the excitation state of the optical mode of H in ZrH_x would
 cause changes in the scattering with the low-energy neutrons.

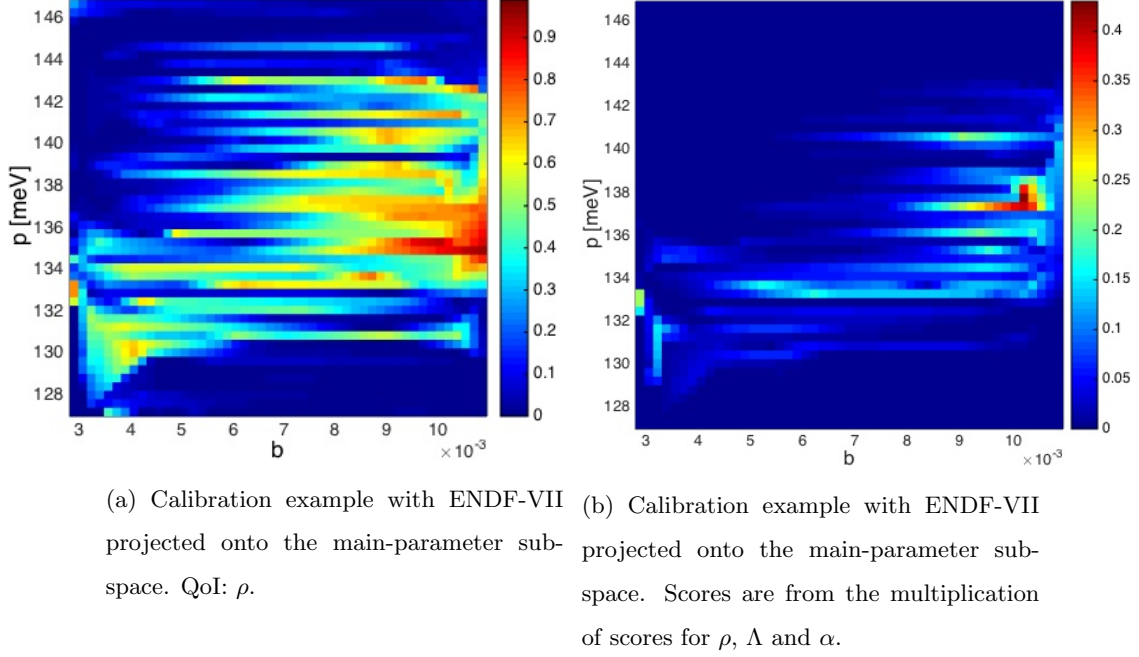


Figure 6: Calibration with multiple QoIs.

there exist gaps in the calibrated parameter scores. This creates an irregularly-shaped high-score region that is imprinted with the set of samples from parameter space. The intuitive way to avoid or mitigate the data gaps would be to increase the sample numbers of the parameter combinations and generate many sets of scattering data to run MCNP simulations and gain smoother and more continuous score distributions. Nevertheless, the computational expense could be insurmountable to reach this goal. Therefore, it is reasonable to develop methods to effectively perform the calibration without necessitating a dense sampling of the input space. The methods should be able to give smooth score distributions when appropriate and must be computationally affordable.

One possible approach is to create a map from the inputs to the outputs from limited numbers of simulations. Assuming the inputs X and simulation outputs Y_i , where the subscript i denotes a QoI, are subject to relationships

hidden in the code (e.g. MCNP in this case), we want to establish a model for the mapping $f : X \mapsto R$ such that

$$Y_i = f(X) + \epsilon_i, \quad X \in D \quad (9)$$

where ϵ_i is a random error and D is the input parameter space. Such a model is sometimes called an emulator or, alternatively, a surrogate model. Moreover, given inputs, we also expect the emulators to generate outputs informed by probabilistic distributions representing the confidence in the results, with which we could apply the scoring strategy developed for direct calibration. Some Bayesian inferred emulators hold these properties. Candidates in this work are Gaussian process regression (GPR) and Bayesian multivariate adaptive regression splines (BMARS) inspired by their performances in radiation-hydrodynamics experiments in McClarren et al's work[19], among others.

4.1. Gaussian process regression

Gaussian process regression generates distributions of functions (emulation outputs) which interpolate the output data in the training dataset. A Gaussian process (GP) is a collection of random variables. Any subsets of such collection has a joint Gaussian distribution. GP defines the mapping (the regression model) from the inputs to the outputs, i.e. $f : X \mapsto R$, to be fully specified by a mean function $\mu(X)$ and a covariance function $k(X, X')$ (also called “kernel”):

$$f(X) \sim \mathcal{GP}(\mu(X), k(X, X')) \quad (10)$$

where $f(X)$ is the function value at location X in the input space and the covariance function k specifies the covariance between the pair of random variables (X, X') in the input space.

And it is often assumed that the error is subject to a normal distribution with user-defined variance σ_n^2 :

$$\epsilon_i \sim N(0, \sigma_n^2), \quad (11)$$

therefore Y_i in Eq. (9) obeys

$$Y_i \sim GP(\mu(X), k(X, X') + \delta_{XX'} \sigma_n^2) \quad (12)$$

where $\delta_{XX'}$ is the Kronecker delta. In practice, one is free to choose the type of the kernel. In this paper, we choose to use fully squared exponential kernel, shown in Eq. (13), to assure smoothness of the emulation outputs [19]. This kernel is given by

$$k(X_i, X_j) = \sigma_f^2 \exp \left\{ -\frac{1}{2} (X_i - X_j)^\top (\mathcal{D}^{-1})^2 (X_i - X_j) \right\} \quad (13)$$

where the σ_f^2 is the maximum value of the covariance. \mathcal{D} is a diagonal parameter matrix. It is usual to write $\theta = \{\sigma_f, \sigma_n, \mathcal{D}\}$ as “hyperparameters”, which would not be user-designated, but be calculated in the procedure of building the emulator[20]. The parameters of the kernels are estimated in the Bayesian inference procedure (see, for instance Ref. [20]). Then the covariance matrix element between two different input points can be calculated as:

$$K_{ij} = k(X_i, X_j). \quad (14)$$

One formulates the predictions contingent upon the training data by:

$$f^*|f \sim N(\mu^* + K^{*\top} K^{-1}(f - \mu), K^{**} - K^{*\top} K^{-1} K^*) \quad (15)$$

where the quantities X , f , X^* and f^* are the training set inputs, corresponding function values, modeler-defined input values (test input) and predictions at the input points (or point sets for multi-D cases) from GPR, respectively. Additionally, $K_{ij} = k(X_i, X_j)$, $K_{ij}^* = k(X_i^*, X_j)$ and $K_{ij}^{**} = k(X_i^*, X_j^*)$. Therefore, GPR generates a Gaussian distribution with a mean and a covariance at each points we designated for interest.

Figure 7 is an example of GPR emulation. The dot points are generated from a logistic function with normal errors. The GPR emulator, as observed, follows the trend of data to infer the underlying function, GPR also generates interpolated function distributions informed by normal distribution; the variance in the distribution this is used to infer the uncertainty in the fit.

4.2. Bayesian Multivariate Adaptive Regression Splines (BMARS)

For this paper, we choose BMARS as a candidate emulator as well as GPR. BMARS arose originally from multivariate adaptive regression splines (MARS)

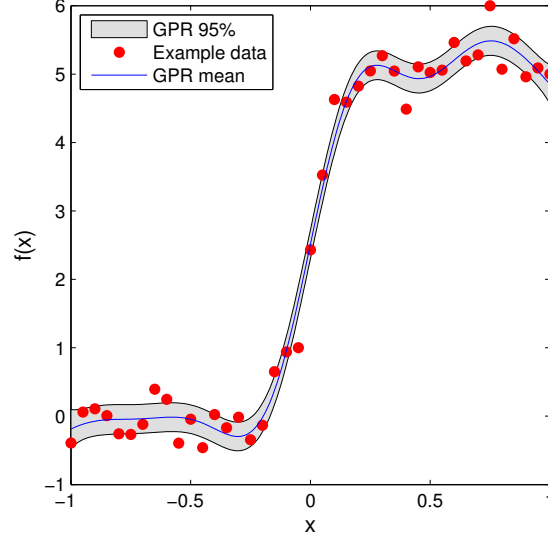


Figure 7: Example of GPR 1D data fitting for a logistic function.

developed by Friedman[21]. MARS is a curve-fitting technique which emulates the relationship between the inputs and outputs as a summation of spline functions at different orders[22]. In the 1D case, the spline functions are defined to be continuous and polynomial functions at some order on part of the domain and zero otherwise. Multivariate splines are simply multiplications of 1D spline functions. MARS linearly combines those splines to construct bases functions. Following the same notations in Ref. [19], Eq. (16) shows an example of basis function:

$$B_i(X) = \begin{cases} 1 & i = 0 \\ \prod_{j=1}^{J_i} [s_{i,j}(X_{v(i,j)} - t_{i,j})^{r_i}]_+ & i = 1, 2, \dots \end{cases} \quad (16)$$

where X is the input matrix, each column of which is an input parameter vector or the interaction of two input vectors, $(\cdot)_+ \equiv \max\{0, \cdot\}$, and $t_{i,j}$ is a knot point.

295 With the $(\cdot)_+$ operator, the splines has nonzero values when the inputs are larger than the knot values. r_i is the order of the spline function. Index $v(i,j)$ gives the split on knot $t_{i,j}$; $s_{i,j}$ is the sign indicator.

Then with those basis functions, the MARS estimated f can be expressed by:

$$f(X) = \sum_{i=0}^I \beta_i B_i(X), \quad (17)$$

where β_i is the coefficient or weight associated with the i^{th} basis function $B_i(X)$ [23, 22].

300 Denison et al. introduced Bayesian MARS (BMARS) that generates a posterior distribution of predictive MARS function[24]. The estimations of making inference of the posterior predictive distributions involves a Markov chain Monte Carlo process (MCMC).

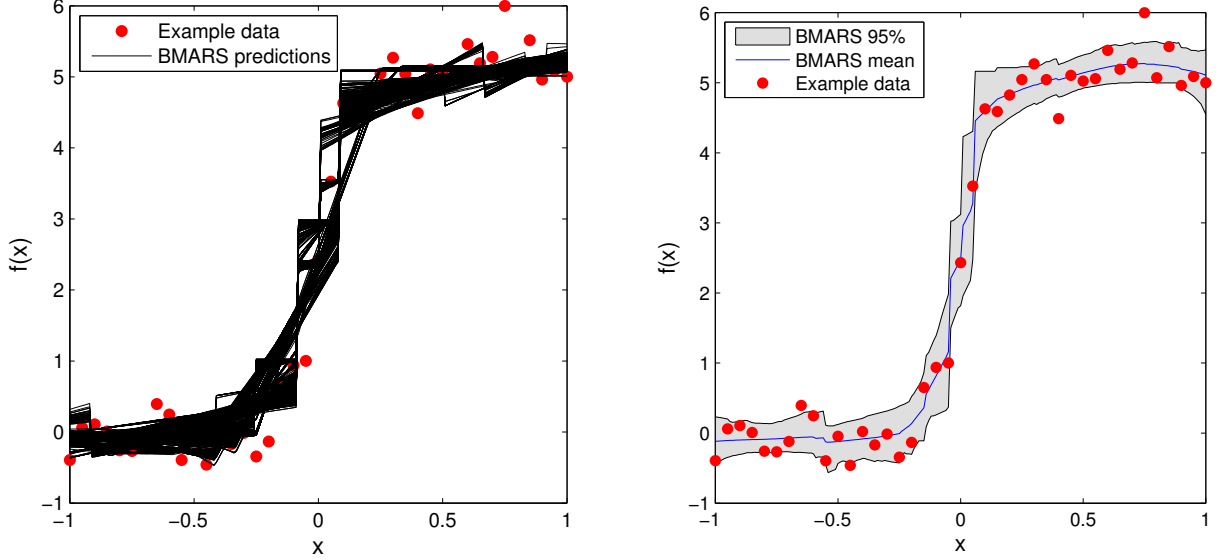
Figure 8a shows several predictions sampled from posterior distributions. 305 And Figure 8b is the example of prediction data with 95 % confidence interval. It is noted that BMARS results in distributions asymmetric about the mean prediction. Although both BMARS and GPR interpolate functions with distributions, BMARS generate finite samples of the interpolants, while GPR has a continuous functional form for the distribution. This implies one does not get
310 a simple expression for the predictions for each input set.

4.3. Emulation based calibration

The application of emulators in calibration would not change the protocol described in Figure 3. The only change is the method we apply in Step 5 for calibration. Instead of direct calibration, we train the emulators with simulation
315 results to gain a mapping from the inputs to the outputs. With modeler defined inputs, emulators generate predictive outputs from a mapping. Then, we can score the emulated results and project them onto the defined input parameter meshes and find the desired calibrated parameter sets.

4.4. Calibration implementation

320 Since GPR generates predictions given by a normal distribution, fortunately, the scoring algorithm developed for direct calibration could directly be applied to GPR emulated results (see Figure 5).



(a) Example of BMARS 1D data fitting. (b) Example of BMARS 1D data fitting
The regression models are drawn in MCMC (with 95 % confidence interval).
procedure when inferring.

Figure 8: Example of BMARS 1D data fitting for the logistic function.

However, BMARS emulated results, which are not subject to normal distributions, disable the application of the original scoring strategy. This drives us
 325 to develop an alternative method. Since BMARS generate a set of samples from
 distributions as shown in Figure 5, somewhat similar with GPR's distributed
 results, it is natural to come up with generating an discrete probability distribu-
 tion (histogram) with those samples and then calculating the overlap between
 each realized output and the experimental or measured distribution. Figure 9 is
 330 an example for scoring in such way. One of the benefits is that the modeler
 does not need to know the analytical form of the emulation distribution. The
 BMARS emulation results do not need to be assumed as Gaussian, which does
 not necessarily hold.

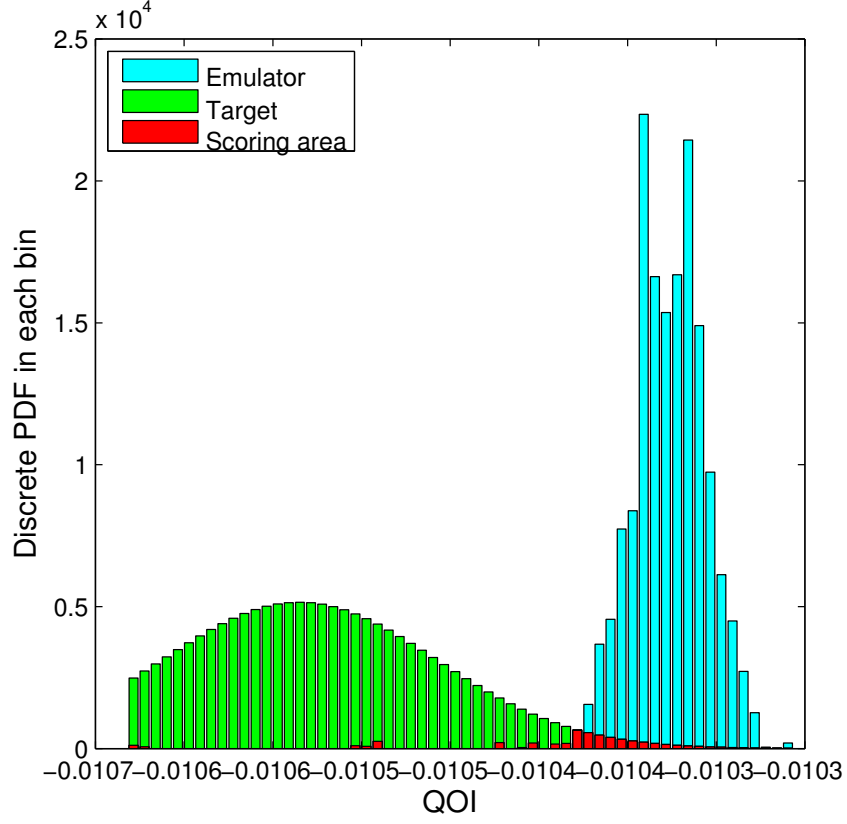


Figure 9: Scoring example with BMARS emulated QoI.

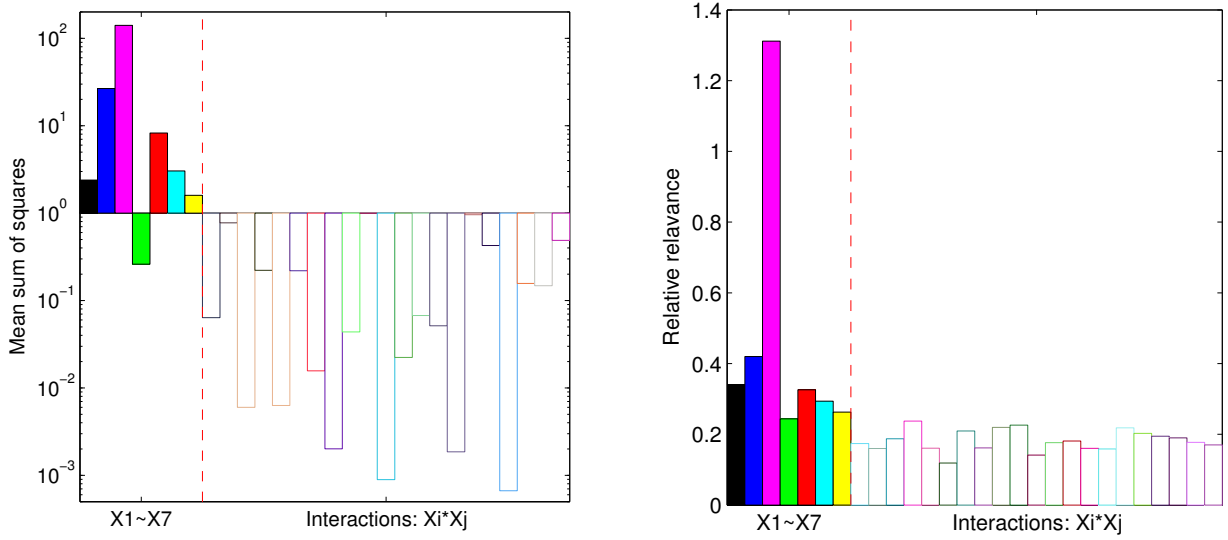
4.5. GPR based calibration results

335 4.5.1. Significant parameter selection

As stated earlier, not all seven parameters are necessarily needed to gain plausible models fitting the simulation data. To rule out the insignificant members, several techniques could be employed. GPR has the capability of testing the significance of inputs to outputs[19]. The diagonals of Λ are the characteristic length scales, which measure the responsiveness of outputs to input vectors

340

if inputs and outputs are standardized before modeling.⁴ With such standardized inputs and outputs, the reciprocals of scale lengths of matrix Λ measures the significances of corresponding input parameters⁵[19]. As an example, Figure 10 show the comparison between the GPR informed significances (relative relevance) and ANOVA informed significances (mean sums of the squares) of the parameters on reactivity ρ . X_1 through X_7 denotes the standardized forms of FWHM, b , p , T_H , T_{Zr} , r and c , respectively. Basically, both results show b and p (which are X_2 and X_3 , respectively.) are the most important two parameters, especially p (X_3).



(a) Parameter significances (mean sums of squares) from ANOVA analysis. (b) Parameter significances (relative relevance) from GPR emulation.

Figure 10: Parameter significance comparisons from different methods.

⁴Denote the standard deviation and mean of random variable X by σ and μ , respectively, then the standardized form of X is $\hat{X} \equiv \frac{X-\mu}{\sigma}$. The standardization of variables enables one to measure different variables in the same scale.

⁵McClarren et al. used “relative relevance” for the diagonal reciprocal, we continue to use the same terminology in this paper

350 Another possible way of performing significance discrimination is to score
 based on emulations with all seven parameters. The score measures relative
 significance of the parameters. Projecting the scores into the parameter space
 would reveal the sensitivity of the QoIs to parameters qualitatively and clearly.
 Score distribution would form preferences in the subset of significant inputs
 355 and give a uniform calibrated distribution for an insignificant parameter. An
 example is the calibration with all seven parameters. The scores are projected
 on 2D parameter planes as illustrated in Figure 11. Apparently, the high score
 regions of p , the H optical mode peak, are always strictly limited, while for other
 parameters other than b , the H acoustic mode branching ratio, the high scores
 360 spread uniformly over the possible ranges. In other words, for parameters other
 than p and b , randomly picking a value in the parameter's range would not result
 in significant change in simulation results. Specifically for b in Figure 11b, the
 high score region jointly distributes showing the dependence on both b and
 p , which actually demonstrate the results from ANOVA and shrink our input
 365 parameter space from 7 to 2.

4.5.2. GPR based significant parameter calibrations

Figure 12 is the calibration result with GPR emulator. As expected, cali-
 brating with emulated QoIs, with only introducing two significant parameters
 in the model, generate smooth and continuous scoring results. Also, the score
 370 distribution is much flatter. Nevertheless, qualitatively, the high score region
 remains similar to that from direct calibrations. The high scores are centered
 around the region with b of 0.01 and p of 138 meV, the result is consistent with
 direct calibration.

4.6. BMARS based calibration results

375 As the calibration results in Figure 13 show, BMARS calibrates the paramete-
 rs around the same high-score region indicated by direct calibration and GPR.
 The shape of the BMARS scoring result is irregular compared with GPR. The
 high scores remain near the region with b of 0.011 and p of 137 meV, differing

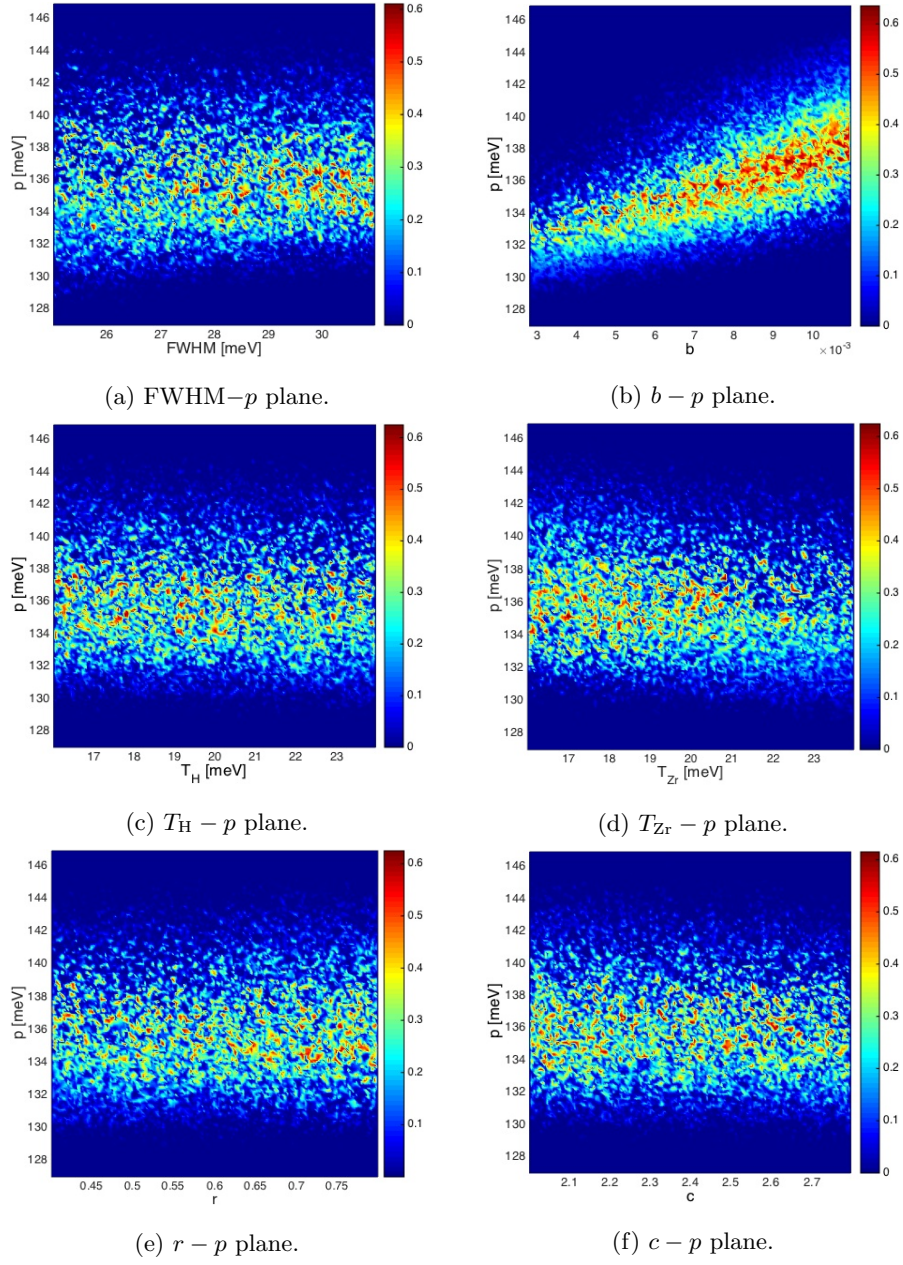


Figure 11: The scores from GPR-based calibration with 7 parameters projected onto two-dimensional planes.

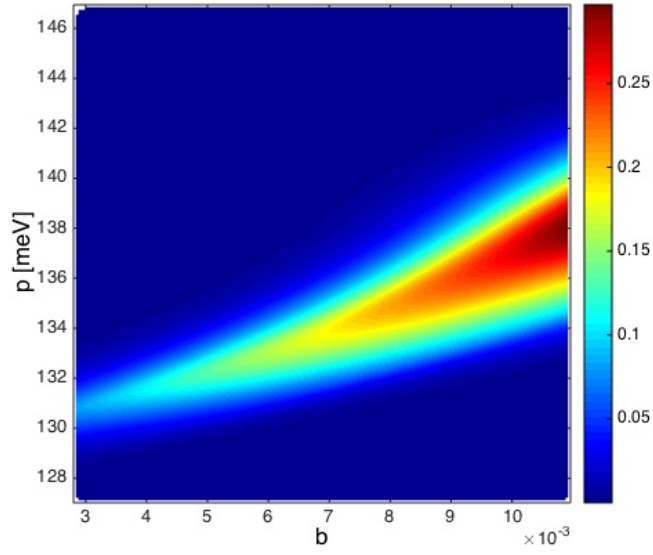


Figure 12: Calibration with GPR.

from GPR's p of 138 meV. And though the calibrated p value is close to the
 380 direct calibration result, the b , however, is a little larger.

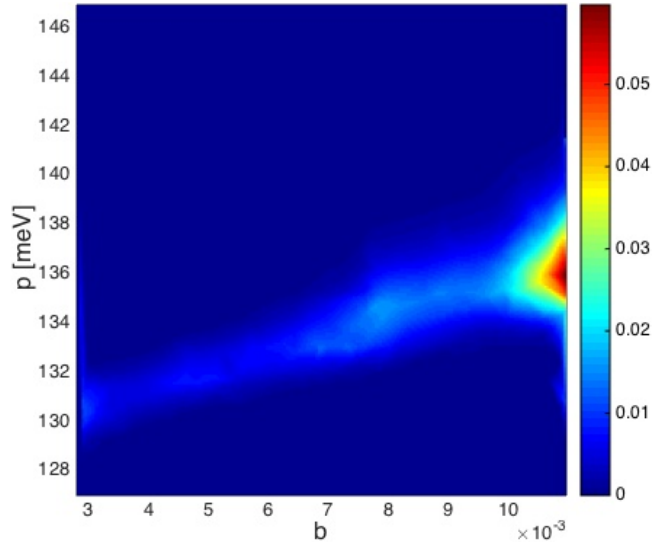


Figure 13: Calibration with BMARS.

4.7. Discussions on emulation based and direct calibrations

Both GPR (Figure 12) and BMARS (Figure 13) emulators achieve the goals set forth above. Both emulators fill give scores $b-p$ pairs without the data gaps as shown in the direct calibration results in Figure 6b. In spite of the satisfactory
385 results from the emulators, the attendant computational cost increase due to constructing and running the emulator is almost trivial (within one hour on a single PC). This compares to the tremendous increase of cost if more MCNP simulations were needed to increase the parameter sample size.

5. Tests for emulation calibrated parameters

390 5.1. Calibrated parameter samplings

Although the projections of the scores onto the main-parameter plane show similar spatial shapes, it is still critical to test if the calibrated parameter distributions will result in robust calibrations to surrogate experiments through the process of data generation and simulation. All of these calibration strategies,
395 including the direct calibration, indicate a branching ratio around 0.01. However, the phonon spectrum of H in ZrH_x used in ENDF, which is suggested by Slaggie, indicate a value of $1/241 \approx 0.00415$ [2].

For the purpose of testing the performance of high-score parameter subsets, 28 samples were drawn from the calibrated distributions. A rejection sampling
400 technique was applied over the two main parameters according to the score distribution. Meanwhile, we sample uniformly over the other five parameters with LHS. Then following Step 1 through 4, MCNP generates simulation results. Figure 14a and 14b show the comparisons of the sampling ranges of the main parameters before and after calibration based on GPR and BMARS, respectively.
405 One observation is that the samples from the calibrated parameters from each emulators sharply shrink the sampling ranges, as expected.

5.2. MCNP posteriori tests for calibrations

MCNP tests with GPR- and BMARS-calibrated parameters are shown in Figure 15 and 16, respectively. Overall, calibration processes shrink uncertain-

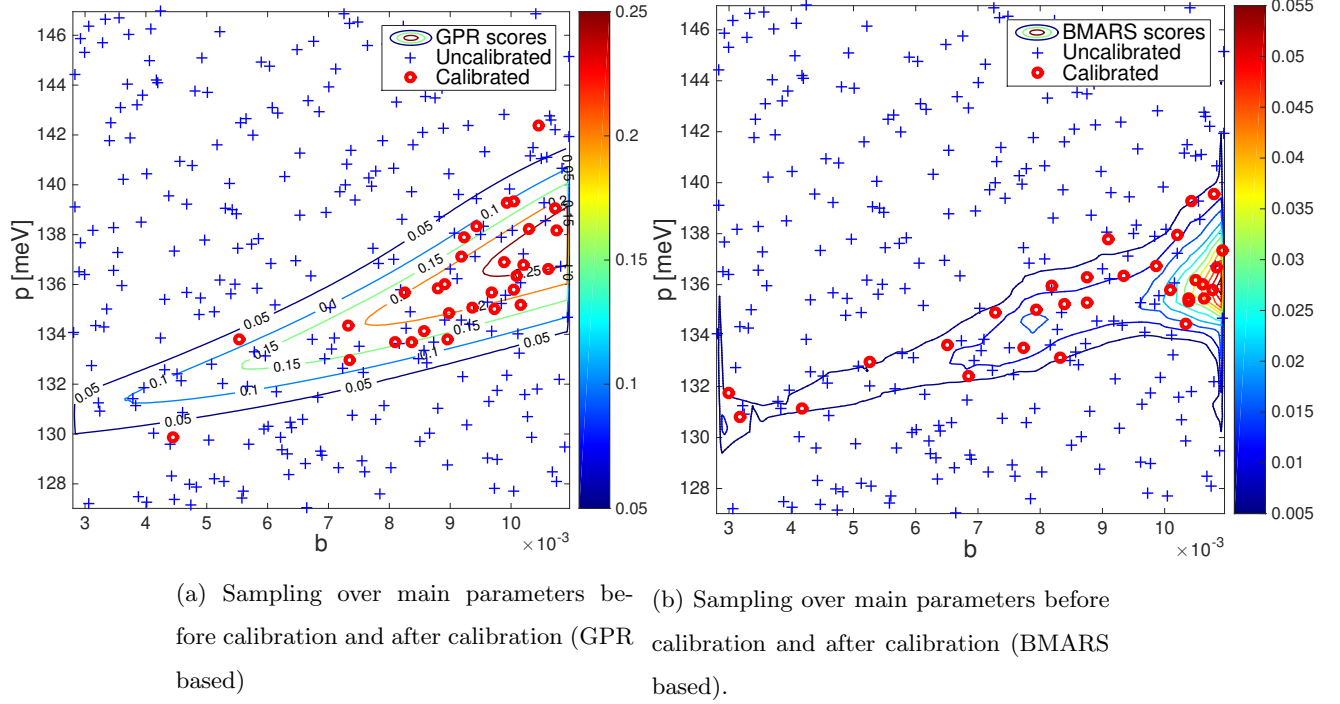


Figure 14: Sampling of main parameters based on different emulators.

ties of three QoIs to different extent while surrounding the surrogate experimental results. Furthermore, though the GPR- and BMARS-based calibration process are carried out by different emulators, the calibrated parameters present comparable calibrated distributions of the QoIs. These results are tabulated in Table II. Ranges of the mean QoI shrink. As do the standard deviations of the QoI means, e.g. the standard deviation of reactivity at room temperature shrinks from 0.13716 \$ to around 0.03 \$ with both emulators.

A more practical question is: what if we can only afford one case to run for testing the calibration. This would be close to the real scenario for a full-scale system. This fact motivated us to check if the calibrated parameter set with the highest-score is accurate. Fortunately, as shown in Table III, both the BMARS based and GPR based test results, which are named “Highest-score sample”, stay within one or two standard deviations of the surrogate experimental values.

Table II: Reference, uncalibrated and calibrated results comparison

		α_T [\$/K]	Λ [s]
Mean (Std.)	Surrogate experiments	-0.01054 (0.00008)	7.47508 (0.00194) $\times 10^{-5}$
	Uncalibrated	-0.01051 (0.00025)	7.48043 (0.00770) $\times 10^{-5}$
	GPR calibrated	-0.01055 (0.00010)	7.47738 (0.00353) $\times 10^{-5}$
	BMARS calibrated	-0.01057 (0.00012)	7.47808 (0.00322) $\times 10^{-5}$
Nominal range	Uncalibrated	$-0.01111 \sim -0.00970$	$7.46060 \sim 7.49767 \times 10^{-5}$
	GPR calibrated	$-0.01088 \sim -0.01034$	$7.47151 \sim 7.48241 \times 10^{-5}$
	BMARS calibrated	$-0.01074 \sim -0.01030$	$7.47234 \sim 7.48511 \times 10^{-5}$
		ρ_{600K} [\$]	
Mean (Std.)	Surrogate experiments	-0.11085 (0.01695)	
	Uncalibrated	-0.12151 (0.07266)	
	GPR calibrated	-0.09612 (0.02679)	
	BMARS calibrated	-0.09493 (0.02667)	
Nominal range	Uncalibrated	$-0.27897 \sim 0.09072$	
	GPR calibrated	$-0.15246 \sim -0.04771$	
	BMARS calibrated	$-0.14938 \sim -0.04001$	

Table III: Reference, uncalibrated and highest-score sample comparisons

QoIs		α_T [\$/K]	Λ [s]
Mean (Std.)	Surrogate experiments	-0.01054 (0.00008)	7.47508 (0.00194) $\times 10^{-5}$
Highest-score Sample (Std.)	GPR calibrated	-0.01051 (0.00007)	7.47729 (0.00194) $\times 10^{-5}$
	BMARS calibrated	-0.01062 (0.00007)	7.48013 (0.00202) $\times 10^{-5}$
Nominal range	Uncalibrated	$-0.01111 \sim -0.00970$	$7.46060 \sim 7.49767 \times 10^{-5}$
QoIs		ρ_{600K} [\$]	
Mean (Std.)	Surrogate experiments	-0.11085 (0.01695)	
Highest-score Sample (Std.)	GPR calibrated	-0.09852 (0.01540)	
	BMARS calibrated	-0.10161 (0.01695)	
Nominal range	Uncalibrated	$-0.27897 \sim 0.09072$	

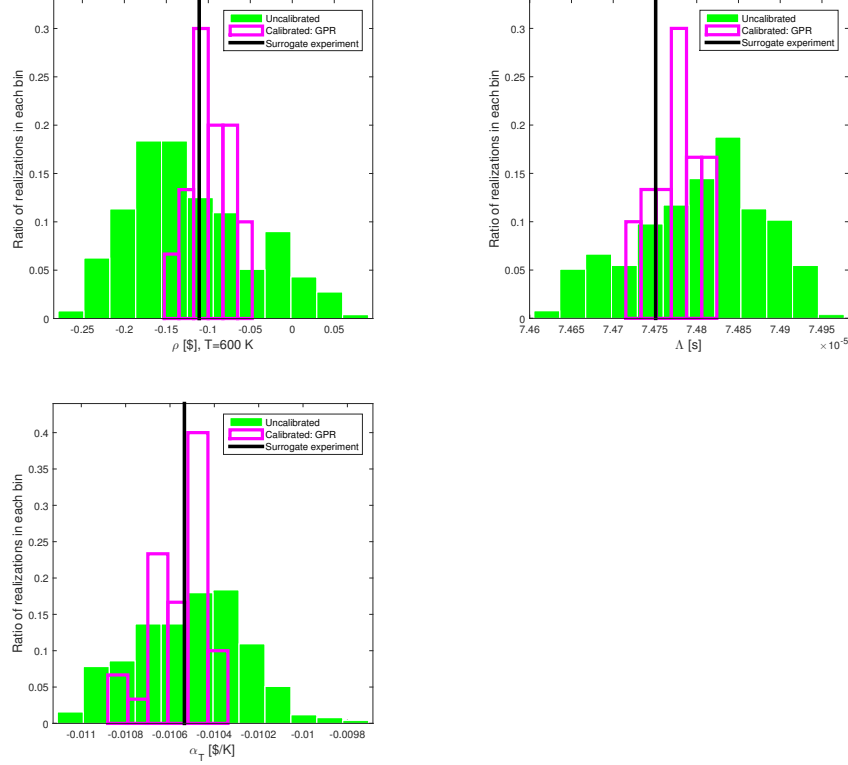


Figure 15: MCNP tests for GPR based calibrations.

5.3. Extrapolated test

We calibrated the PPS parameters with ρ_{600K} , α_T and Λ_{600K} . Since the
425 scattering data for the surrogate experiment is from ENDF, which is based
upon using a single phonon spectrum for all temperatures[3], it is reasonable to
hypothesize that the thermal scattering data with calibrated PPS model param-
eters, which means the same phonon spectrum, at 600 K shall result in accurate
simulation posterior distributions for QoIs at 293.6 K as well. Figure 17 presents
430 the reactivity at 293.6 K simulated with data before calibration and after cali-
bration. The uncertainties of both results decrease as expected. Corresponding
results are tabulated in Table IV.

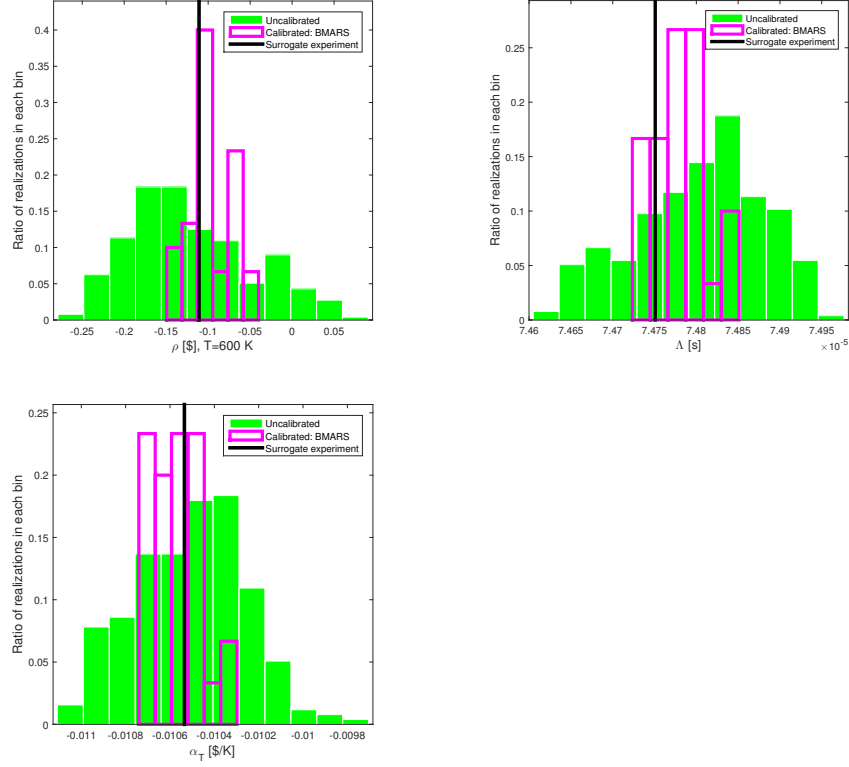


Figure 16: MCNP tests for BMARS based calibrations.

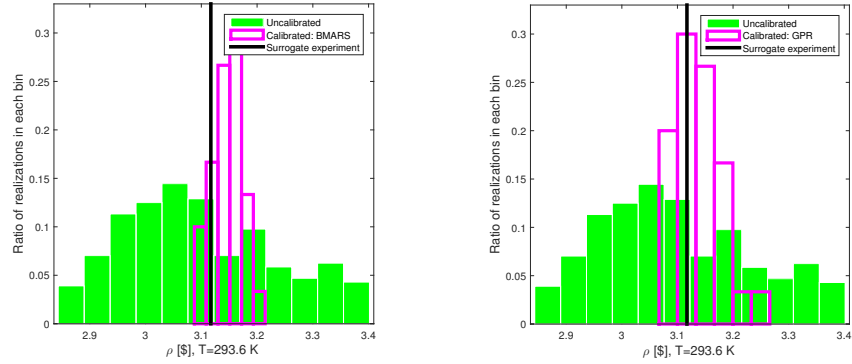


Figure 17: Extrapolation tests for ρ at $T = 293.6$ K using calibrated parameters from QoIs calibrated at 600 K.

Table IV: Reference, uncalibrated and highest-score sample comparisons

QoI		$\rho_{293.6K}$ [\$]
Mean (Std.)	Surrogate experiments	3.11708 (0.01658)
Highest-score Sample (Std.)	GPR calibrated	3.12151 (0.01477)
	BMARS calibrated	3.15399 (0.01476)
Nominal range	Uncalibrated	2.84338 \sim 3.40155
	GPR calibrated	3.06685 \sim 3.26608
	BMARS calibrated	3.08754 \sim 3.21448

6. Concluding remarks

6.1. Summary

Previously, we established a seven-parameter phonon spectrum model for ZrH_x in TRIGA reactor. Based on this model, we sampled the parameters, generated thermal scattering data of ZrH_x and performed criticality simulations. Also, we used TRIGA reactor simulations as a surrogate experiment. In the process, we developed scoring algorithm to estimate the similarities between the simulations and the surrogate experiment. Then a calibration framework for the parameters of the parameterized phonon spectrum models based on the scores was established.

In this work, we extended the calibration framework. Instead of estimating the scores using simulation results, we invoked emulators, in particular Gaussian process regression and Bayesian multivariate adaptive regression splines, to emulate the mapping from the proposed parameters to the QoIs. Scoring is performed based upon estimating similarities of the surrogate experiment and emulation results at designated input parameter points. When projecting the scores into parameter space, it is noticed that both emulators narrowed the preferred parameter sets down. Posteriori criticality test results with parameters sampled based on the scores resulted from both emulators illustrate the effectiveness of the extension of the calibration framework. Uncertainties of the QoIs narrow down to different extent, e.g. the range of mean values of ρ_{600K} change

from $[-0.27897, 0.09072]$ \$ to $-0.14938 \sim -0.04001$ \$ (BMARS based) and
455 $-0.15246 \sim -0.04771$ \$ (GPR based).

We also extended the posteriori test with the thermal scattering data produced with the same phonon spectra used in 600 K to room temperature (293.6 K) as an example of an extrapolation experiment. We found the the using the parameter ranges calibrated at 600 K were still accurate at room
460 temperature.

Though the emulation based framework accomplished the aforementioned goal, there remain uncertainties in the simulations used in our calibrations. The MCNP simulations were carried out with large numbers of particles such that the statistical error of each simulation QoI is much smaller than the total
465 variations of QoIs. In such a case, the mean values of QoIs are used as the input of the emulators to emulate the mapping from input to output without affecting the calibration accuracy. Nonetheless, this would not be true when the uncertainties of simulation QoIs are not negligible. In such a case, using the nominal means of simulation QoIs as emulation inputs would introduce
470 noticeable statistical errors. In such a case we would need to account for the uncertainty in the simulation results.

Though the calibration framework developed here is based on ZrH_x in a TRIGA reactor, the methodology is not limited to that system. We believe that the framework could also be applied to the materials with thermal scattering,
475 e.g., water, in light water reactors (LWRs).

6.2. Future work

We investigated three types of sensitive QoIs in this work at 600 K. To further constrain the calibration, more sensitive QoIs are needed. We previously investigated the total absorption rates over the whole energy range of ex/in-
480 core neutron detectors and claimed the insensitivity of such QoIs to the phonon spectrum [11]. Yet, recent, more detailed simulations indicate that detectors measuring only the thermal flux will be sensitive to our parameters. This observation should not be a surprise since when we manipulate the phonon spectrum,

the thermal scattering cross sections are changed, which results in the variation
485 of the up-scattering and thus the thermal flux[10, 9]. We believe monitoring
the thermal absorption rate with detectors could bring in another constraint
besides the ones used in this paper. Such in-core thermal neutron detectors will
be available soon in the Texas A&M TRIGA reactor.

Also, the temporal impact of varying phonon spectrum of ZrH_x in appli-
490 cations such as pulse experiments should be investigated and corresponding
calibration work should be done for TRIGA reactors.

Acknowledgments

This project is funded by Department of Energy NEUP research grant from
Battelle Energy Alliance, LLC- Idaho National Laboratory, Contract No: C12-
495 00281. The authors would like to thank the anonymous reviewers of this work
for their thoughtful comments that served to make this a stronger paper.

References

- [1] Safety Analysis Report, Tech. Rep. 05000128, Nuclear Science Center,
Texas A&M University (2011).
- 500 [2] E. L. Slaggie, Central Force Lattice Dynamical Model for Zirconium Hy-
dride, J. Phys. Chem. Solids 29 (1968) 923–934.
- [3] R. E. MacFarlane, D. W. Muir, The NJOY Nuclear Data Processing Sys-
tem Version 91, Tech. Rep. LA-12740-M, Los Alamos National Laboratory
(1994).
- 505 [4] R. E. MacFarlane, New Thermal Neutron Scattering Files for ENDF/B-
VI, Release 2, Tech. Rep. LA-12639-MS(ENDF 356), Los Alamos National
Laboratory, Los Alamos, NM (1994).
- [5] S. S. Malik, D. C. Rorer, G. Brunhart, Optical-Phonon Structure and Pre-
cision Neutron Total Cross Section Measurements of Zirconium Hydride,
510 J. Phys. F: Met. Phys 14 (1984) 73–81.

- [6] A. C. Evans, D. N. Timms, J. Mayers, S. M. Bennington, Neutron-Scattering Study of the Impulse Approximation in ZrH_2 , *Phys. Rev. B* 53 (1996) 3023–3031. doi:10.1103/PhysRevB.53.3023.
URL <http://link.aps.org/doi/10.1103/PhysRevB.53.3023>
- 515 [7] M. D. R. Badea, C. H. M. Broeders, On the Impact of Phonon Spectrum Shifts of the Hydrogen Binding in ZrH , in: International Conference on Nuclear Data for Science and Technology 2007, no. 242, 2008. doi:10.1051/ndata:07681.
- 520 [8] M. Mattes, J. Keinert, Thermal Neutron Scattering Data for the Moderator Materials H_2O , D_2O and ZrH_x in ENDF-6 Format and as ACE Library for MCNP(X) Code, Tech. Rep. INDC(NDS)-0470, Institute for Nuclear Technology and Energy System (IKE)-University of Stuttgart (2005).
- 525 [9] W. Zheng, R. G. McClarren, Physics-Based Uncertainty Quantification for ZrH_x Thermal Scattering Law, in: ANS Winter Meeting 2013, Vol. 109, ANS, 2013, pp. 743–745, washington, D.C., November 10 - 14.
- [10] W. Zheng, Physics-based uncertainty quantification for ZrH_x thermal scattering law, Master’s thesis, Texas A&M University (December 2013).
- 530 [11] W. Zheng, R. G. McClarren, Effective Physics-Based Uncertainty Quantification for ZrH_x Thermal Neutron Scattering in TRIGA Reactors, in: PHYSOR 2014-The Role of Reactor Physics Towards a Sustainable Future, no. 1104568, PHYSOR, 2014, the Westin Miyako, Kyoto, Japan, September 28 - October 3, on CD-ROM (2014).
- [12] G. I. Bell, S. Glasstone, Nuclear Reactor Theory, 3rd Edition, Krieger Pub Co, Princeton, NJ, 1985.
- 535 [13] R. L. Iman, Latin hypercube sampling, Encyclopedia of quantitative risk analysis and assessment.
- [14] J. F. Briesmeister, MCNP: A General Monte Carlo N-Particle Transport Code, Tech. Rep. LA-12625-M, Los Alamos National Laboratory (1993).

- [15] E. W. Weisstein, ANOVA, <http://mathworld.wolfram.com/ANOVA.html>,
540 [Online; accessed 10-Oct.-2013] (2008).
- [16] D. D. Wackerly, W. Mendenhall, R. L. Scheaffer, Mathematical Statistics with Applications, 7th Edition, Cengage Learning Inc., Belmont, CA, 2008.
- [17] T. J. Santner, B. J. Williams, W. Notz, The Design and Analysis of Computer Experiments, Springer Series in Statistics, Springer, New York, NY,
545 2003.
- [18] J. Cohen, Statistical Power Analysis for the Behavioral Sciences, L. Erlbaum Associates, 1988.
URL <https://books.google.com/books?id=Tl0N21RA09oC>
- [19] R. G. McClarren, D. Ryu, R. P. Drake, M. Grosskopf, D. Bingham,
550 C.-C. Chou, B. Fryxell, B. van der Holst, J. P. Holloway, C. C. Kuran, B. K. Mallick, E. Rutter, B. R. Torralva, A physics informed emulator for laser-driven radiating shock simulations., Rel. Eng. & Sys. Safety 96 (9) (2011) 1194–1207.
URL [http://dblp.uni-trier.de/db/journals/ress/ress96.html#](http://dblp.uni-trier.de/db/journals/ress/ress96.html#McClarrenRDGBCFHHKMRT11)
555 [McClarrenRDGBCFHHKMRT11](http://dblp.uni-trier.de/db/journals/ress/ress96.html#McClarrenRDGBCFHHKMRT11)
- [20] C. Rasmussen, C. Williams, Gaussian Processes for Machine Learning, Adaptive Computation and Machine Learning, MIT Press, Cambridge, MA, USA, 2006.
URL <http://mitpress.mit.edu/026218253X>
- [21] J. H. Friedman, Multivariate adaptive regression splines, Ann. Statist.
560 19 (1) (1991) 1–67. doi:10.1214/aos/1176347963.
URL <http://dx.doi.org/10.1214/aos/1176347963>
- [22] H. Stripling, R. McClarren, C. Kuran, M. Grosskopf, E. Rutter, B. Torralva, A calibration and data assimilation method using the
565 bayesian {MARS} emulator, Annals of Nuclear Energy 52 (0) (2013) 103 – 112, nuclear Reactor Safety Simulation and Uncertainty Analysis.

doi:<http://dx.doi.org/10.1016/j.anucene.2012.08.025>.

URL <http://www.sciencedirect.com/science/article/pii/S0306454912003453>

- 570 [23] A. Chakraborty, B. K. Mallick, R. G. McClarren, C. C. Kuranz, D. Bingham, M. J. Grosskopf, E. M. Rutter, H. F. Stripling, R. P. Drake, Spline-Based Emulators for Radiative Shock Experiments With Measurement Error, *Journal of the American Statistical Association* 108 (502) (2013) 411–428. [arXiv:http://dx.doi.org/10.1080/01621459.2013.770688](http://dx.doi.org/10.1080/01621459.2013.770688),
575 doi:10.1080/01621459.2013.770688.

URL <http://dx.doi.org/10.1080/01621459.2013.770688>

- [24] D. G. T. Denison, C. C. Holmes, B. K. Mallick, A. F. M. Smith, *Bayesian Methods for Nonlinear Classification and Regression*, Wiley, 2002.

URL <http://www.wiley.com/WileyCDA/WileyTitle/productCd-0471490369,descCd-tableOfContents.html>
580